https://doi.org/10.15407/ufm.25.02.213

M.O. VASYLYEV [1,*], E.M. RUDENKO [1,], and S.M. VOLOSHKO [2,***]**

[1] G.V. Kurdyumov Institute for Metal Physics of the N.A.S. of Ukraine,
36 Academician Vernadsky Blvd., UA-03142 Kyiv, Ukraine

[2] National Technical University of Ukraine
'Igor Sikorsky Kyiv Polytechnic Institute',
37 Peremohy Ave., UA-03056 Kyiv, Ukraine

* vasil@imp.kiev.ua, vasil1934@ukr.net,
** voloshkosvetlana13@gmail.com, *** emrudenko@ukr.net

INFLUENCE OF THE LOW-ENERGY INERT-GAS ION BOMBARDMENT ON THE STRUCTURE AND PROPERTIES OF METALLIC THIN FILMS

The goal of the review is to analyse the main published results of the most systematic studies of changes in the structural–phase state, the physical and chemical properties of the metallic single- and multilayer thin films' systems after bombardment by the low-energy (<10 eV) inert-gas ions. Nanoscale film systems are obtained using two widespread physical methods: magnetron deposition and thermal resistive evaporation. The single-layer systems are based on such pure metals as Co, Cu, Ni, Pt, Nb, Ti, Fe, and W. The films deposited on the Si(100) substrate have thicknesses in the range of 25–700 nm. Multilayered thin films are fabricated based on the following combinations: Cu/Ni, Ni/Cu/Cr, Cr/Cu/Ni, and Ni/Cu/V with 25–30 nm thickness of each layer. The low-energy inert-gas ions' (Xe^+, Ar^+, Ne^+, He^+) bombardment with varying beam energy in the range of 200–10 000 eV and fluence in the range of 10^{15}–10^{19} ions/cm^2 are used. The ion bombardment-induced morphology, microstructure and chemical evolution of the polycrystalline thin films are studied using x-ray diffraction (XRD), secondary ion mass spectrometry (SIMS), Auger-electron spectroscopy (AES), electrography, transmission electron microscopy (TEM), scanning electron microscopy (SEM), atomic force microscopy (AFM), and tribological tests. Different physical mechanisms contributing to this evolution and their relation to theoretical models and experimental studies of the ion-induced thin films are discussed.

Keywords: thin films, ion bombardment, surfaces, phase transformations, wear resistance.

Citation: M.O. Vasylyev, E.M. Rudenko, and S.M. Voloshko, Influence of the Low-Energy Inert-Gas Ion Bombardment on the Structure and Properties of Metallic Thin Films, *Progress in Physics of Metals*, **25**, No. 2: 213–242 (2024)

1. Introduction

The metallic single-layer and multilayer thin film systems are extensively used in basic science and numerous applications in high-tech industries because of their excellent physical and engineering properties. It has been established that they exhibit improved electronic, magnetic and mechanical characteristics compared with bulk metal materials and are successful in magnetic heads, microelectromechanical systems (MEMS), nanoelectronics, microsensor technology, and spintronics devices. The development of thin-film synthesis methods with a wide range of predefined properties is a very important task of materials science, which is due to the specifics of their formation technology. The properties of such materials are determined by the methods and kinetics of their condensation and are derived from their morphology, as well as the perfection of their crystal and electronic structure. As is known, the most important stages of condensation of the thin film compositions from the gas medium or in the vacuum are the processes of adsorption and adhesion [1–13].

Thin metal films based on Cu are extensively used in modern electronic devices as interconnecting metal because of their unique high electrical and thermal conductivity, as well as resistance to electromigration properties. However, Cu interdiffuses into Si substrate and causes the deterioration of p–n junctions used in electronic devices. To prevent such an interdiffusion effect the Ni diffusion barrier is used [8, 9]. Currently, the increased interest in Cu-based film systems has been also associated with photovoltaics, where Cu is one of the most promising candidates for replacing the high-cost Ag paste contacts, which are used in about 90% of solar cell devices. However, the modern trend towards smaller contact sizes for nanoelectronic devices is accompanied by the long-term reliability issues associated with such effects as adhesion, diffusion, and oxidation of the film materials. One of the conventional approaches to stabilize these effects and improve the corrosion properties of Cu film is the use of additional functional layers, which leads to the formation of multilayer thin-film systems.

Currently, to modify the conductive materials' properties, two conventional energy ranges of the neutral gas ions are used. The high-energy ions (>10 eV) lead to changes in the bulk properties of the materials [14–18]. Unlike high energy, the low energy (<10 eV) inert gas ion bombardment is connected more with morphological, microstructure and electronic changes of the surface or near-surface region of the massive materials [19–22]. The low-energy inert-gas ion beam is commonly used in the various methods of materials surface analysis, for example, in the Secondary Ion Mass Spectrometry (SIMS) [23–25]. Nowadays, low-energy inert-gas ion bombardment of the material surface is widely used in various fields of science and technology. As an example, we note ion beam-assisted phys-

ical or chemical deposition coatings and thin films for improving both adhesion behaviour and physicochemical properties [26–29]. This is very important to achieve the high technological level of the micro- and nanodevice systems because the ion-beam modification of the materials makes it possible to change the physicochemical, mechanical, electrical and magnetic properties, the fine structure of the materials' surface [30–32]. The range of low beam energies (<3 keV) is of high interest for modern nanotechnologies to restrict the radiation damaging the surface structure. The low-energy inert-gas ion beam sputtering is widely used for surface patterning, surface cleaning and depth profiling of the materials. Correspondingly, the focus of the ion beam research shifted recently from the fundamental aspects of ion–solid interaction to surface engineering, mainly to nanostructure technology, novel tribological, corrosion, and optical applications [33–34].

It is well known that the surface chemical activity can be also altered by low-energy inert-gas ion sputtering. It was first shown that catalysts were almost one order of magnitude more efficient after such influence thanks to the emergence of the so-called 'active centres' [35]. A closer examination of the inert-gas ion bombardment influence with incident ion energies of order 1 keV on the surface chemical activity has been performed by the examples of the oxygen–surface with pure metals [36–40]. As reported, the oxygen–surface interactions and the surface kinetic reactivity depend significantly on the optimal relation between the ion energy and the primary ion current density as well as the sputtering rate of the surface composition [22].

The newer interests have evolved in the areas of the low energy ion beam-induced effects of the patterning and self-organisation processes. These include the ripples, the dot formation, the dewetting, and the morphological patterning on the surface [41–44]. It turns out that the local stress on the surface is frequently the important driving force for the self-organization effects, in particular, for the surface pattern formation. In addition, the ion bombardment-induced stress has also been used as a way to control the shape of the thin layer's structures in the microelectromechanical system devices. In addition, the ion beams have been increasingly used as processing tools in preparing nanostructures and smoothing material surfaces, which becomes critical in advancing these applications.

Because the structure and properties of the thin metal films are significantly different from their massive analogues, it is of scientific and practical interest to study the low-energy effect of inert-gas ions on the physical and chemical properties of such materials. Knowledge of such influence mechanisms is of great practical importance in connection with the production of the elemental base on high-tech thin-film nanoelectronics. Using varying the inert-gas ion beam energy in the low-energy interval makes it possible to control the effectively different properties of the

deposited single- or multilayer thin film systems by improving their physical and chemical properties and adhesion processes [45–48].

The goal of the review is to analyse the main results of the most systematic studies of changes in the structural-phase state, the physical, chemical, and mechanical, properties of the single- and multilayer thin film systems bombarded by the low-energy inert-gas ions.

2. Single-Layer Thin Films

2.1. Micro- and Nanostructural Changes

It is known that there are two Co polymorphs, namely, the hexagonal polymorph, which is stable at low temperatures, and the cubic polymorph, which is unstable and is at high temperatures. In Ref. [49], the Co thin films (100 nm thick) were deposited in the transmission microscope column on the glasses by vacuum evaporation at the pressure of 10^{-4} Pa. The thin film samples were ion bombarded directly in the microscope column by Ar^+ ions accelerated to 10 keV and with the ion current density of about 2–3 μA mm^{-2}. It was enabled to observe the microstructure changes in the preferred orientation of the films directly. The experiments [49] led to the formation of the hexagonal Co layers (Fig. 1, *a*). As a result, both in the films that initially displayed the preferred orientation and in those that did not, the microstructure eventually changed after the 4-5 min bombardment to form the cubic Co film with the ⟨110⟩ preferred orientation along the direction of the Ar^+ ions that is favourable for the incident ion penetration (Fig. 1, *b*). According to [49] the thermal and displacement spikes and radiation cause abrupt local temperature increases, which can lead to the material melting followed by drastic quenching. It was expected that at the displacement spikes hexagonal Co would transform into a cubic structure that is stable the high temperatures and will remain quenched after cooling. Consequently, the observed (110) orientation in the cubic polymorph may be explained by the recrystallization mechanism at centres made up of the cubic Co crystals that are preferentially oriented along the ⟨110⟩ direction (along the direction that is favourable for incident ion penetration).

Typical changes in the surface morphology induced by Ar^+ ion (2 and 3 keV) bombardment of the Ag thin film (40 nm thick) were demonstrated in Ref. [50] using Transmission electron microscopy (TEM). Fig. 2 shows the TEM image of the as-deposited film. This image discloses numerous crystallites with diameters in the range of 20–300 nm. In addition, it was observed that the electron diffraction consists of the spotty Debye rings, which correspond to the typical polycrystalline structure with the developed (111) plane. Figure 3 shows the surface morphology for the Ag film bombarded with 2 keV Ar^+ ions. It should be seen that such a film contains the row of the 'voids' indicated by arrowheads. The comparison of Figs 2

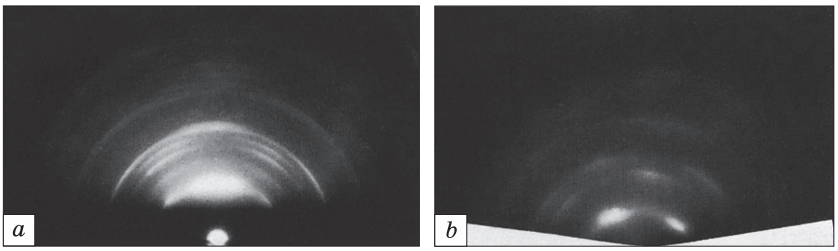

Fig. 1. The electron diffraction pattern of the unbombarded Co film (*a*) and after bombardment with 10 keV Ar^+ ions (*b*) [49]

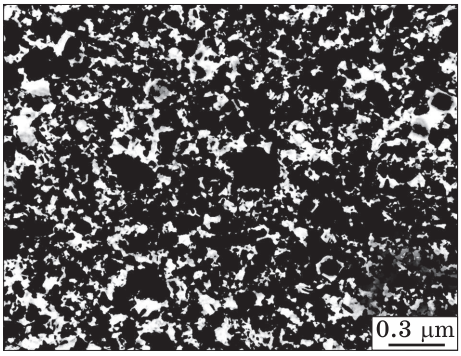

Fig. 2. TEM image of the as-deposited Ag film [50]

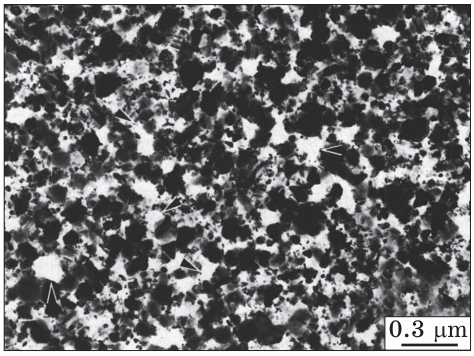

Fig. 3. TEM image of the Ag film ion-bombarded at 2 keV for 3 min [50]

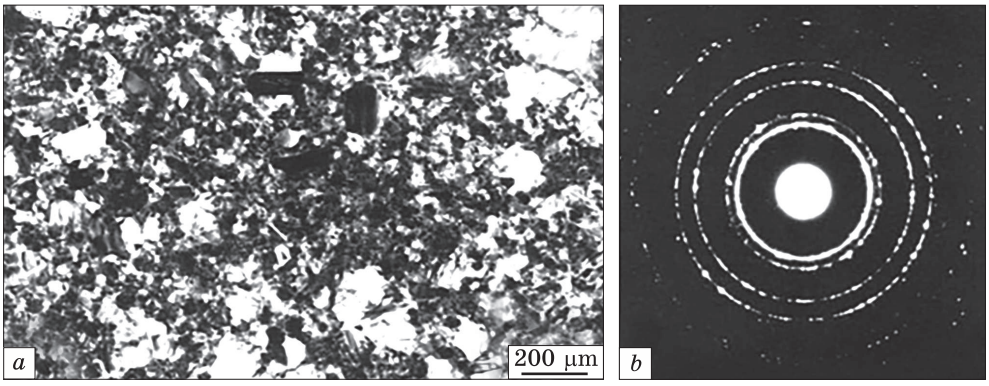

Fig. 4. TEM image (*a*) and corresponding ED pattern (*b*) of the as-deposited Ag film 100 nm thick [51]

and 3 shows that after Ar+ ion-bombarded film the Ag crystallites are larger than those crystallites composing the as-deposited film of the average dimension. This effect is termed as 'ion-induced crystal growth'. Authors [50] allow that the growth of the Ag crystallites is enhanced by

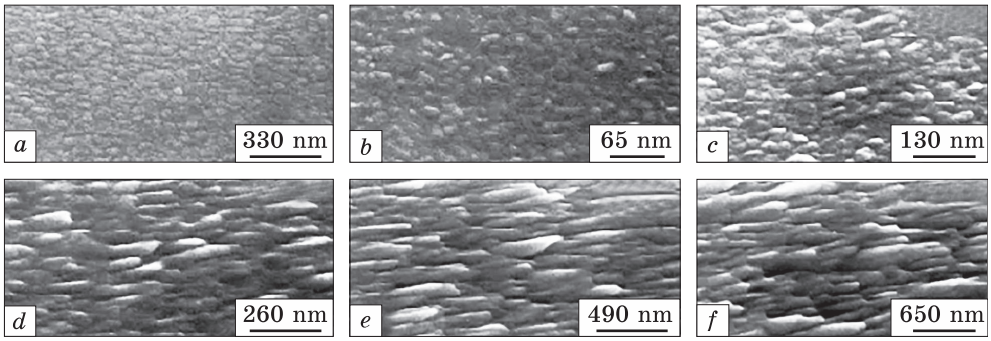

Fig. 5. The SEM images of the sputtered crater centres observed with different resolution viewing at 40° directions with respect to the film surface normal. Ion beam density was 100 μA/cm^2, and the crater depths were estimated from the sputtering rate of ≈23 nm/min [51]

raising ion energy, and presumably, the thermal effect of impacting ions is responsible for the observed effect.

The morphology evolution of ion bombardment-induced microcones on the polycrystalline Ag thin film surfaces bombarded by Ar^+ ions was studied in Ref. [51]. Ag films were deposited on the mirror-polished Si wafers to various thicknesses, using the dc-sputter-deposition technique. The target was bombarded with 3 keV Ar^+ ions and the current densities were in the range of 5–500 μA/cm^2. The Ar^+ ion beam entered the target at 60° concerning the target normal. The microstructure changes were observed using the SEM and the TEM. Figure 4 shows the TEM image of the as-deposited Ag thin film and the corresponding electron diffraction (ED) pattern. As shown in figure (b) by the spotty Debye rings there are numerous crystallites with dimensions in the range of 20–200 nm while the crystallites were randomly oriented. It is also observed that the initial film surface was almost flat without ion bombardment.

In Figure 5, the morphological structures at the bottoms of the bombardment-induced craters produced on the as-deposited Ag film 700 nm thick are shown. These images reflect the following physical process. As noted above the initial film surface is almost flat, but very slightly rough. As concluded in Refs. [53, 54], the ion bombardment should soon flatten such very slight bumps. However, at the very early stage of the ion sputtering, for Ag grains, the three-dimensional growth to roughen the surface slightly happens (Figs. 5, *a*, *b*). This corresponds to the so-called 'ion-induced grain growth' [55]. As the sputtering was prolonged at this stage, grains were still featureless, but they gradually grew into rod-shaped, or cylindrical, projections (Figs. 5, *c*, *d*). When the sputter depth reached ≈300 nm, the rod-shaped projections continued to lengthen. The projections shown in Fig. 5, *d* were ≈50–150 nm in cross-section diameter, and

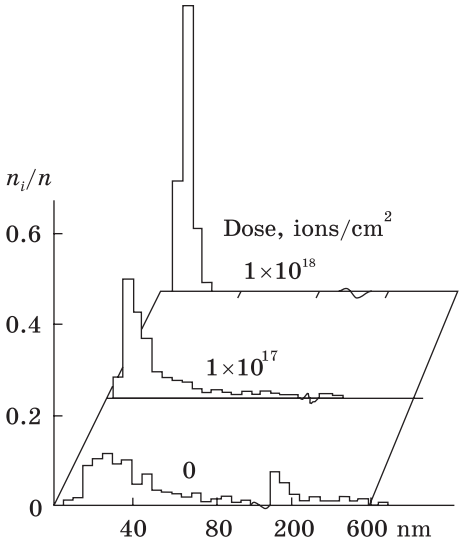

Fig. 6. Histogram of grain size distribution in the polycrystalline Ni initial film (zero dose) and after irradiation by 20 keV He^+ ions up to a dose of 5×1017 and 1×10^{18} ions/cm^2 [56]

several of them — ≈300 nm long. Figs. 5, *e* and *f* demonstrate that if the ion sputtering further continued, the projections stopped to lengthen, but they began to be reshaped into conical structures with rounded tips. It can be noted that there is no great difference was recognized between the average lengths of the rod-shaped and conical projections ultimately constructed (compare Figs. 5, *d*, *f*). In this way, the evolution of the microcones on the Ag film after ion sputtering consisted of the next physical processes: the development of rod-shaped projections and their reshaping into conical microstructures.

There are many of data on the ion bombardment influence on the microstructure of thin metal films. Polycrystalline and single polycrystalline Ni thin films (100 nm thickness) after He+ ion bombardment with energies of 20 keV and ion beam with a current density of (2–3) mkA/cm^2 were studied in Ref. [56]. Using TEM the radiation dose-dependent microcrystalline size distribution was determined (Fig. 6). The given distribution has a long 'tail' aside big grain size date (up to 600 nm). It can be seen that as a result of the ion bombardment with an ion dose of 51×10^{17} ion/cm^2 the region of the grain size values is decreased from 600 to 200 nm and the maximum of the size distribution is shifted to the region 15–20 nm. The higher ion dose (1×10^{18} ion/cm^2) leads to further grain fragmentation and respectively to decreasing of the average grain size to 10–15 nm at the maximal size <30 nm.

In the paper [57] the Cu thin film nanostructures formation on the Si(100) substrate using low energy Ar^+ ion beam bombardment at room temperature was demonstrated. In particular, the morphology evolution mechanism between the self-organized nanoripples' and nanodots' patterns by modulating the Cu layer microstructures was investigated. After deposition, the Cu/Si(100) thin films (55 and 100 nm thick) were bombarded by an Ar^+ ion beam under normal incidence to the sample surface with the ion flux $J < 1.1\times10^{15}$ cm^{-2}s^{-1} and the ion energy 1.2 keV and 2.5 keV. According to θ–2θ XRD patterns, the Cu films deposited on Si(100) substrates have a polycrystalline structure with grains randomly

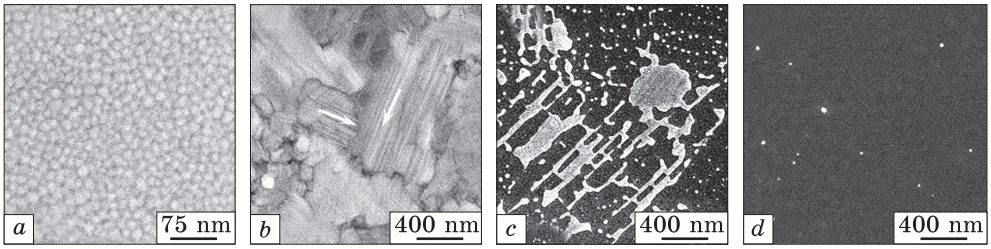

Fig. 7. SEM images of the Cu thin films (110 nm) morphological evolution after bombardment by Ar^+ ions ($J = 1.1 \times 10^{15}$ cm^{-2}s^{-1}, $E = 1.2$ keV): as deposited (*a*), $t = 60$ s (*b*), $t = 180$ s (*c*), $t = 240$ s (*d*). Two white arrows indicate ripple orientation [57]

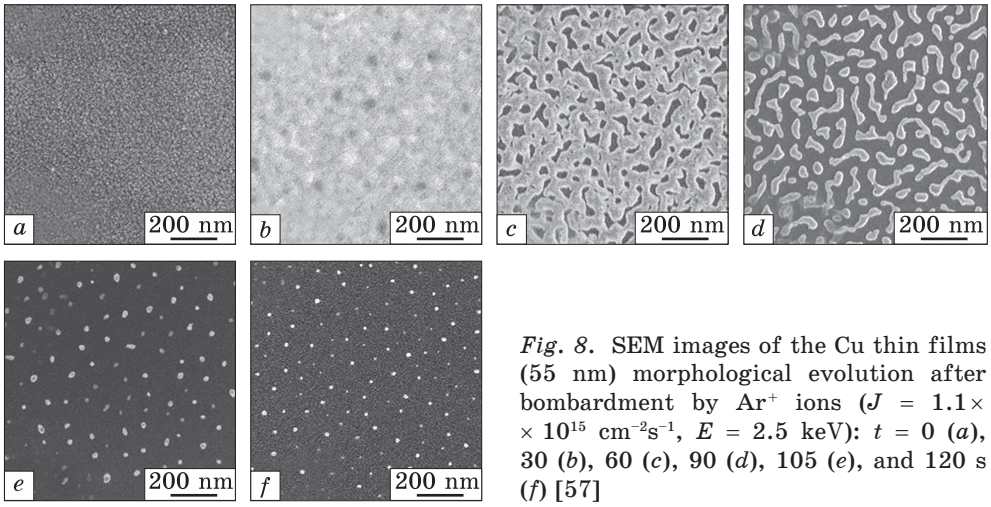

Fig. 8. SEM images of the Cu thin films (55 nm) morphological evolution after bombardment by Ar^+ ions ($J = 1.1 \times \times 10^{15}$ cm^{-2}s^{-1}, $E = 2.5$ keV): $t = 0$ (*a*), 30 (*b*), 60 (*c*), 90 (*d*), 105 (*e*), and 120 s (*f*) [57]

oriented. The longitudinal grain size of the Cu (110 nm) and Cu (55 nm) thin films was estimated to be ≈60 nm and ≈16 nm, respectively. This fact indicates that Cu grains grow rapidly as the film gets thicker. Figure 7, *a* shows the initial surface morphology with a typical bump-like structure. After ion bombardment for 60 s the sub-micrometre grains range can be clearly seen (Fig. 7, *b*). The white arrows on this Figure indicate that the nanoripples were formed on the single-grain surface with ripple orientation randomly distributed. Fig. 7 *b*, *c* demonstrates that after further ion bombardment, the film structures turned to isolated nanoclusters, nanodots and even nanowires. It is interesting that after almost the entire Cu layer was removed, sparsely distributed Cu nanodots were left on the substrate (Fig. 7, *d*).

Figure 8, *a*–*f* shows the morphological evolution of the Cu thin films (55 nm) after bombardment by Ar^+ ions ($E = 2.5$ keV) indicating that the film had nanocrystalline grains. Such treatment leads the initially continuous film to the system of Cu clusters, isolated islands, and nanodots

combined with nanorods. At last, the nearly uniformly distributed nanodots are observed. For example under Ar^+ ion bombardment with $J = 1.1 \times 10^{15}$ cm^{-2} s^{-1} and $E = 2.5$ keV, the Cu nanodots with a mean diameter of 12 ± 4.3 nm, height of ≈5.3 nm and dot-density of 1.8×10^{10} cm^{-2} were obtained. It was noted that reducing the ion dose leads to an increase in the dot density. For the 110 nm thick polycrystalline Cu, it was found that nanoripples' patterns are formed on the Cu grain surface.

2.2. Stress Formation

Several recent studies have considered that ion-induced stress can be the possible driving force for pattern formation on the bombarded bulk material surfaces [58]. Such irradiation-induced stress is important to control the shape of the thin film structures used in microelectromechanical devices [59]. The ion beams have been also used as processing tools to create nanostructures and smoothing surfaces [60]. Knowledge of the mechanisms that induce the ion-induced in the thin film is critical in advancing these applications.

The work [61] is the initial investigation of the stress that is developed in thin metal films bombarded by low-energy ions (Xe^+, Ar^+, Ne^+, He^+). Unlike the previous studies of the effects of high-energy ions (>50 keV), the low-energy ion beams have a much shallower implantation range in the near-surface region. In Ref. [61], Pt films with thicknesses from 15 to 40 nm were grown on 2–2.5 nm thick and 450 nm long Si(001) cantilevers by using sputter deposition. All ion bombardments (0.5 keV, 2 keV) were performed at the room temperature (RM). The incidence angle of the beam was 20° from the surface normal; the ion doses ranged from 2×10^{11} to 5×10^{12} cm^{-2}s^{-1}. Figure 9 presents the initial stress in Pt films as the thickness function. Observed positive stress values correspond to the tensile stress, in particular, in the first 3 nm thickness. In another case, the stress is compressive when the film becomes thicker and reaches the steady state value (–1.27 GPa).

Observed changes of the Pt films stress after bombardment by different types of the ions (2 keV Xe^+, Ar^+, and Ne^+, and 0.5 keV He+), one can see in Fig. 10. For the films bombarded by Xe^+, Ar^+, and Ne^+ there are the similar behaviours, namely, the rapid increase in the tensile stress at the low ion doses bombardment and the smaller constant change in the stress with dose at the higher doses. For the case of Xe^+, the changes in the stress are concentrated within the range of the ions and the tensile stress of 2–3 GPa is derived. For 2 keV ions Ne^+, the initial compressive stress thickness is reduced by the tensile change in the bombarded region. Nevertheless, here, the integral stress in the film remains compressive. It is important to note, that the range of Ne^+ ions is greater than those of Ar^+ and Xe^+ and, therefore, the average increase in tensile stress in the damaged region is thus significantly larger for the film bombarded by the

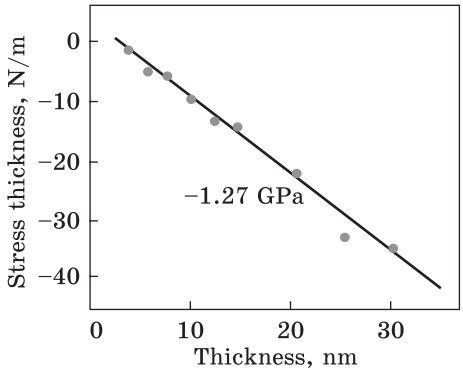

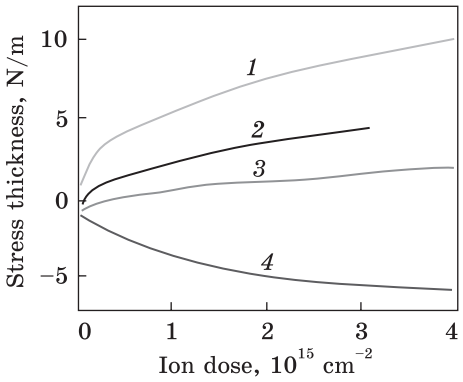

Fig. 9. The distribution of stress throughout the thickness in Pt films [61]

Fig. 10. The change in the stress-thickness of Pt films during ion bombardment: 2 keV Xe^+ (*1*), 2 keV Ar^+ (*2*), 2 keV Ne^+ (*3*), 0.5 keV He^+ (*4*) [61]

ions with higher mass. The results in Ref. [69] show that the mechanism creating the tensile stress in Pt correlates with the damage energy density and not the damage energy or ion range. The behaviour bombardment with lighter He ions shows qualitatively different results. A monotonically increasing compressive stress is induced in the film from the outset of the ion bombardment. The He^+ ions have very low damage energy in Pt and the energy transfer from He to Pt atoms is low, so such a result is perhaps not too surprising for Pt films. As shown in Ref. [19], for the ion energies less than 1 keV, essentially no defects are created during implantation.

In Ref. [61], the major mechanisms that contribute to the observed stress change were demonstrated for heavy inert-gas ions: tensile stress by the melting along the ion track and compressive stress by the incorporation of interstitials into the Pt thin films. It is also possible for the mechanism, which involves interstitial diffusion, can create stress beyond the ion range. The individual mechanisms can be enhanced or suppressed, which results in a wide range of observed effects by varying the initial stress of the film or the mass of the ions. The mechanism caused by the thermal spike is enhanced duty to increase the ion mass or energy. On the other hand, the interstitial mechanism can be suppressed in (111) oriented films by applying the in-plane biaxial compressive stress. In the case of the lighter and low-energy He+ ion, the authors [61] proposed that, unlike the other inert gas, always leads to additional compressive stress in Pt thin films. They also attribute this difference to the light mass of He+ ion since at the energies employed. This type of ion cannot efficiently produce point defects in Pt film by recoil effect, and therefore, He atoms trap to either defect sites or the grain boundaries and lead to compressive stress. Adding to the compressive stress can additionally be possible when He atoms form small bubbles and ‘punch out’ the interstitial loops.

2.3. Changing Catalytic Properties

The authors [62] investigated the evolution of Au thin film morphology by low energy Ar^+ ion plasma treatment as the catalyst for the growth of the single-walled carbon nanotubes (CNTs). The films having a 0.1–5.0 nm thickness range were prepared by electron beam deposition. The Ar plasma with power from 5 to 15 W was ignited between the electrodes by the introduction of the dc voltages at 500 °C. The pressure of the Ar atmosphere was kept to 1.33×10^2 Pa during the 10-minute plasma treatment. In this work, two important results were obtained. First, the dependence of the nanoparticle size in Au thin films on plasma energy has been established. As can be seen from Fig. 11 (curve *1*), for the 0,5 nm thick Au films the mean particle size linearly increased from 1.40 to 2.32 nm for the plasma power of 0 to 15 W, respectively. This effect is the result of sputtering and surface diffusion-related aggregation. It was proposed that the plasma leads to the substrate surface heating due to the energetic ion impact through the plasma sheath formed in the surface front and accelerates the ion collision energy according to the potential difference existing between the plasma and the film. At the same time, it was shown (1.0 nm in Fig. 11, curve *2*) that the mean particle size of the thicker films decreased at the lower plasma power regime due to the sputtering, then, increased again at the highest plasma power as a result of the diffusion-induced aggregation of the films.

The next important result of the authors [62] is related to the study of the efficient catalyst of the Au nanoparticles obtained from the plasma-treated for the growth of single-walled CNTs by the thermal chemical vapour deposition with the methane source. It was concluded that the optimum condition for CNT growth was observed for the 0.5 nm thick films and the plasma power of 5 W. Figure 12 shows the morphology of the CNTs growth results obtained from the Ar^+ plasma treated 0.5 nm thick Au film using different plasma power.

The kinetics of the adsorbed oxygen layers obtained on the surface of the 100 nm thick Nb, Ti, Fe, Ni, and Cu thin films after bombardment by Ar^+ ions with the wide dose range using the SIMS was studied in Ref. [63]. Thin films (targets) were obtained by deposition in one vacuum cycle ($P = 10^{-5}$ Pa) on the CT-50-1 sitall substrate by electron beam evaporation. The recording of the singly charged positive secondary ions cur-

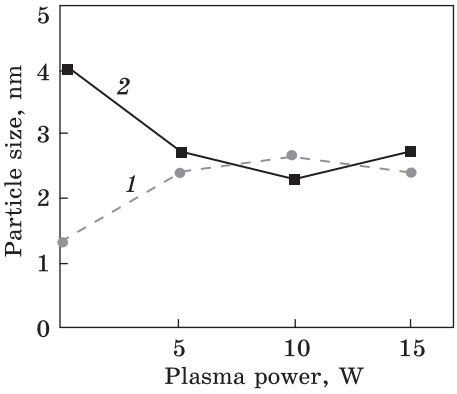

Fig. 11. Variation of Au-particle size as the function of the plasma power applied with 0.5 nm (*1*) and 1 nm (*2*) thick Au films [62]

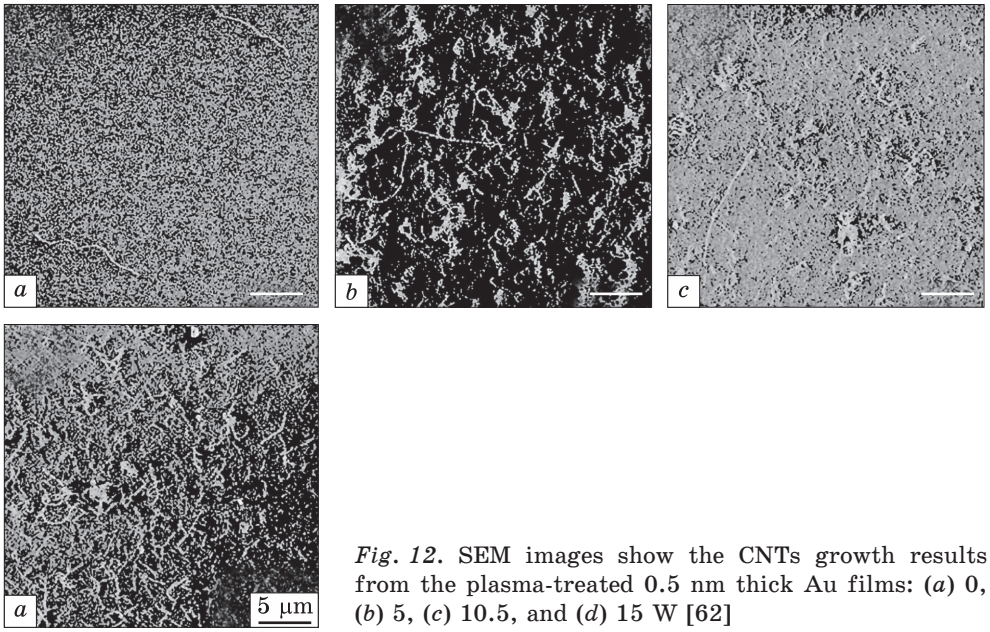

Fig. 12. SEM images show the CNTs growth results from the plasma-treated 0.5 nm thick Au films: (*a*) 0, (*b*) 5, (*c*) 10.5, and (*d*) 15 W [62]

rent of the corresponding metal stable isotopes was carried out using a mass spectrometer. The targets were bombarded by Ar^+ ions with the energy of 4 keV in the wide range of the irradiation doses ($D = 10^{14}$–10^{19} ions·cm^{-2}). The primary ion beam current on the target was 10 μA at the current density of 1.5 μA/mm^2). The initial yield of the secondary ions, as is known, depends significantly on the surface chemical state and can change by several orders of the magnitude of the process of the electronegative atoms adsorption, in particular, oxygen. This physical-chemical effect is the basis of the SIMS application to study the adsorption kinetics and the initial stages of the massive metal samples' surface oxidation [64–66].

As established in Ref. [63], the amplitude of the change in the Ar^+ ion current of the metal ions and its kinetics during sputtering of the metal target surface after oxygen adsorption depends on the dose of the previous ion bombardment, as well as the density of the primary ions beam. Figure 13 shows the kinetic curves for the number of the transition thin metal films obtained by sputtering the surface layer formed as the result of the natural oxidation. When sputtering oxide layers on the surface of the investigated metal films, the sharp increase in the ion emission can be identified at the initial moment (I^+_{max}) of bombardment (h-burst of the secondary ion emission) followed by its decline to the stable level (I^+_{stab}). In this case, the value $h = I^+_{max} - I^+_{stab}$ can serve as the quantitative estimate of the adsorption effect. If one compares the change in the h value and the formation enthalpy of the corresponding oxides, it can be noted that the growth of h

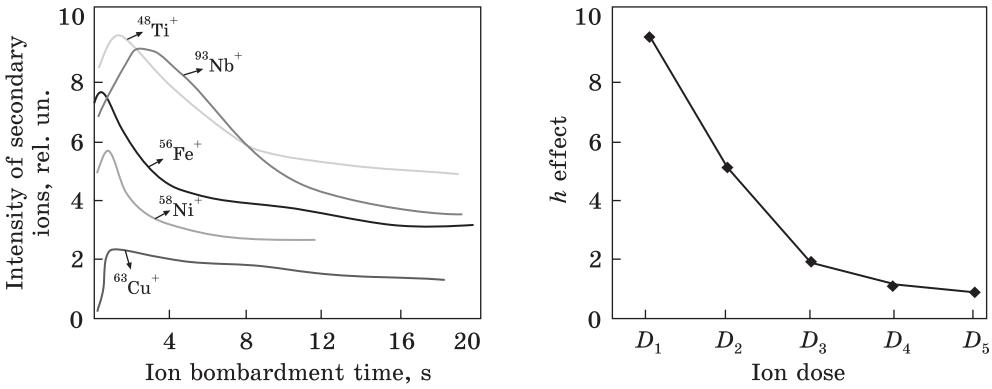

Fig. 13. Dependences of the secondary ions intensity on the sputtering time of the natural oxide layer formed on the Ti, Nb, Fe, Ni, and Cu thin films [63]

Fig. 14. Representative dose dependence of the *h* effect for the Ti film, where $D_1 = 10^{14}$, $D_2 = 10^{16}$, $D_3 = 10^{17}$, $D_4 = 10^{18}$, $D_5 = 10^{19}$ ion·cm^{-2} [63]

correlates well with the value of this thermodynamic characteristic (ΔH, kJ/mol): Ti — 989, Nb — 872, Fe — 570, Ni — 448, Cu — 162. Thus, during ion sputtering of the oxide layers on the investigated metals, two types of the change kinetics in *h* are realized. Kinetics of the 1st type is characterized by the sharp increase in ion emission at the initial moment of bombardment (burst of emission) followed by its decline to the stable level (Ti, Nb, Fe and Ni films). The 2nd-type kinetics is characterized by the presence of an insignificant difference between the initial burst and the stable emission level (Cu film).

The typical dependence of the h effect on the bombardment dose on the example of the Ti film is shown in Fig. 14. For all investigated targets, the maximum passivation effect is observed in the range of bombardment doses $D_3 = 10^{17}$, $D_4 = 10^{18}$, and $D_5 = 10^{19}$ ion·cm^{-2}. The insignificant intensity of the initial burst at the indicated doses is caused by the influence of the oxygen from the residual atmosphere of the vacuum chamber. At lower doses, the effect of the secondary ions emission can be associated with the presence of the oxide layers on the target surface, formed when pure oxygen is injected and partially dispersed by ion bombardment. With the ion sputtering of the oxide layer, the h effect decreases to the minimum level. The observed passivation effect at the metal thin films was explained as the result of the bombardment by the inert-gas ions at doses greater than $D = 10^{16}$ ions·cm^{-2} caused by the change of the structural defect state at the surface layer, which leads to the significant change in the mechanism and kinetics of the oxygen adsorption.

2.4. Implantation Effects

In the study [67], the effect of 5 keV He^+ ion bombardment on thin (about 200.0 nm) aluminium films was presented. The main task of this work was to measure the content of the implanted He atoms on the bombardment dose. Fig. 15 illustrates the retention curve for He atoms implanted at 5 keV, normal incidence, into an aluminium film at room temperature (*a*) and 120 K (*b*) using the Rutherford backscattering technique. It was concluded that the below-saturation retention levels (expressed as the percentage of the incident beam ion dose) are 19% for room temperature bombardment and 24% for 120 K and the saturation levels of the He atoms for the two temperatures are 3 and 4.5 at.% respectively.

2.5. Electrical Resistance Change

The electrical resistance of the thin films Ag, Au, Ti, and W (10.0-50.0 nm) after energetic Ar^+ ions bombardment was studied in Refs. [68, 69]. The dimensions of such polycrystalline films were 1.0 cm long by 0.5 cm wide and of thickness ranging from 10.0 to 50.0 nm. The films were subjected to Ar^+ ion bombardment, with ion energies fixed between 250 eV and 5 keV and doses up to 10^{17} ions/cm^2. For example, Fig. 16 demonstrated the fractional resistance changes (R/R_0) behaviour for the Au films of different thicknesses post-bombarded by Ar^+ ion with energy of 450 eV as the function of the integrated ion dose. As can be seen from these results, during the initial stages of the ion impact for the films of thickness greater than 15 nm the resistance decreased. At higher ion doses, the resistance increased and reached close to the saturation effect. All of the above behaviour was obtained in a greater or lesser degree for the films of Ag, Au, Ti, and W, of thickness from 10 to 50 nm and for all ion energies between 250 eV and 4 keV. Ti film, in particular, showed a very rapid initial rise in resistance after bombardment, but, again, the resistance increased to a steady

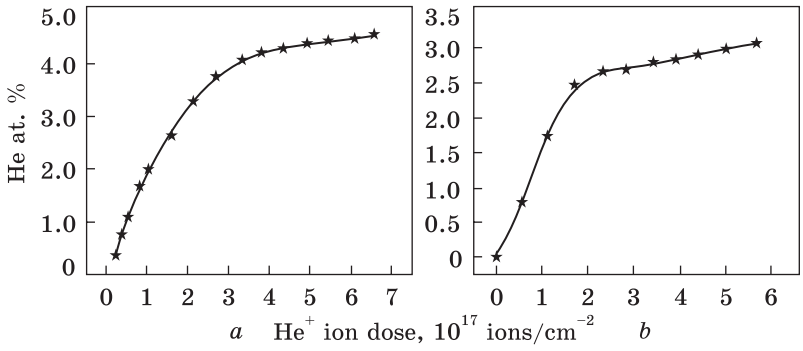

Fig. 15. Retention dose dependence for He atoms concentration at the room temperature (*a*) and 120 K implantations [67]

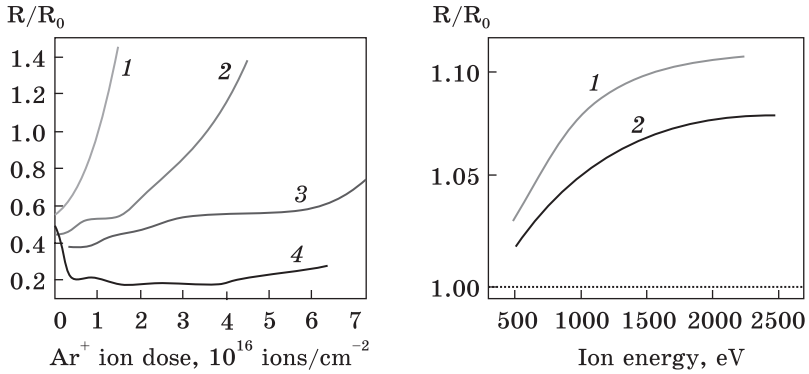

Fig. 16. The fractional resistance (R/R_0) change of Au thin film at different thicknesses after Ar^+ 450 eV ion bombardment for different film thickneses: 11 nm (*1*), 15 nm (*2*), 21 nm (*3*), and 27 nm (*4*) [68]

Fig. 17. The same as in the previous figure but R/R_0 as a function of Ar^+ ion energy for the two initial film thicknesses: 0.1–25 nm (*1*) and 0.2–35 nm (*2*) [68]

value. In Figure 17, the resistance change behaviour is shown as the function of Ar^+ ion energy for two initial film thicknesses. It can be seen that larger resistance changes are observed in the thinner film. It is assumed that this effect is due to film damage since such a damaged layer would occupy a larger fraction of the thinner film thickness. Three stages in the resistance change/ion dose relation were observed [68]. The first at the low ion doses, where the resistance falls, is believed to be the result of the contaminant gas removal from the surface. The next stage at higher ion doses, where the resistance increases to the quasi-constant value, is believed to be associated with damage production near the film surface. At still higher ion doses, the resistance increases to infinity because of the film sputtering.

The resistance of the tantalum thin films of 40–18 nm in thickness, composed of the mixture of tantalum and tantalum oxide, after bombardment with 20 keV Ar^+ ion was investigated in Ref. [70]. For example, Fig. 18 presents the resistance behaviour of the bombarded film as of the ion dose function for films of 50 nm in thickness. It is important to note that the initial resistivity is much greater than that reported for pure tantalum.

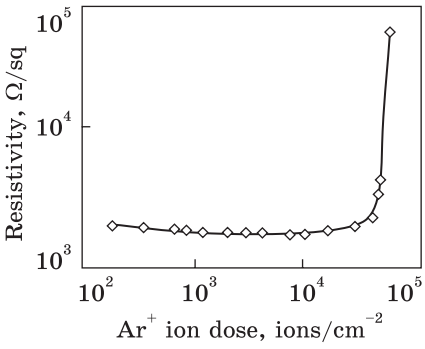

Fig. 18. The surface resistance *(i.e.* resistance per square) *vs.* the ion bombardment dose for tantalum thin film (50 nm thickness) [70]

The argon-bombarded film showed a gradual drop in the resistance up to a dose of 6×10^{16} ions/cm^2 and then a gradual rise, until at doses greater than 2×10^{17} ions/cm^2 the rise became very sharp. As noted in Ref. [70], the resistance increases by five orders of magnitude for the 1% increase in the ion bombardment dose and the resistance dependence on the ion dose is divided into three regions (low, medium and high dose). At the same time, the assumption is made that at the low doses the resistance drops, probably as the result of the gas desorption, whilst at the high doses the resistance rises rapidly due to complete removal of the film due to cascade sputtering processes.

2.6. Change of Optical Characteristics

In Ref. [71], the effects of the low energy He^+ ion (4 keV) on the Au thin films used as the mirror were investigated. The main aim of this experiment is to simulate the action of the solar wind ions on the optical properties of the mirror coatings during long-term missions operating in an environment close to the sun. The mirror coatings are widely used for high reflectance in the vacuum ultraviolet (VUV) and visible (VIS) spectral

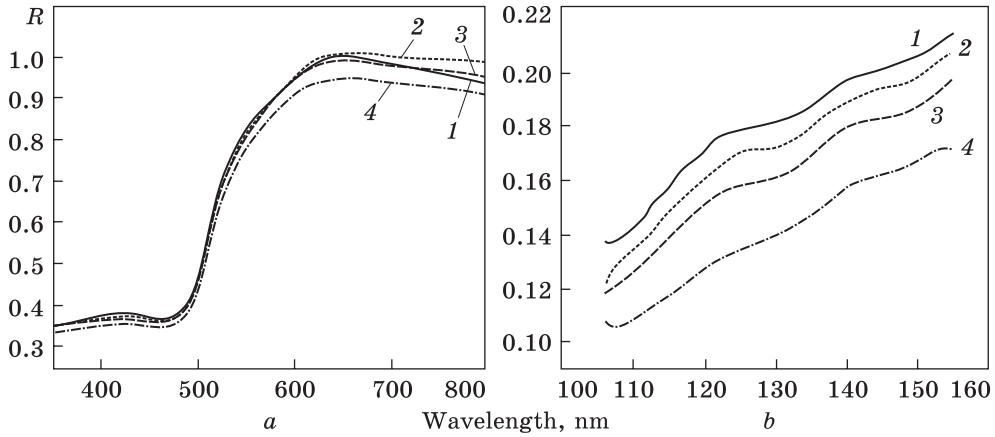

Fig. 19. Reflectance of Au mirrors in the visible (*a*) and the VUV (*b*) spectral range: Au0 (*1*), Au1 (*2*), Au2 (*3*), and Au4 (*4*) [71]

Table 1. **Experimental parameters of the He^+ ion bombardment [71]**

	Films Au1 (1 year fluence)	Films Au2 (2 years fluence)	Films Au4 (4 years fluence)
Duration	5 h	10 h	20 h
He^+ energy	4 keV	4 keV	4 keV
He^+ flux	1.5×10^{11} s^{-1}cm^{-2}	1.5×10^{11} s^{-1}cm^{-22}	1.5×10^{11} s^{-1}cm^{-2}
Total fluence	2.6×10^{15} He^+/cm^2	5.2×10^{15} He^+/cm^2	1.1×10^{16} He^+/cm^2

range. The Au 220 nm thick thin films were deposited by the electron-beam vapour deposition on the p-type Si polished wafer. The He+ ion fluencies were chosen to simulate the effects of respectively of the different years' missions. The experimental parameters, such as sample labels, ion fluence, and energies are shown in Table 1 [71]. The films Au0 were kept untreated as the reference ones.

The reflectance of the Au thin films before and after ion bombardment was measured in the spectral regions: in the visible range (300–800 nm) and the VUV-range wavelength near the Lyman-α line of the solar emission spectrum (121.6 nm). Results of the optical reflectance measurements performed for all the spectral regions and the Au thin films are presented in Fig. 19, *a*, *b*. These data show that the observed reflectance (*R*) decreases with the increase of the ion fluence. Such an effect is stronger for the VUV spectral data. The authors [71] explain the observed optical effects by changing the film surface morphology and the plasmonic effects at the surface as the result of the bombardment by He^+ ions. Degradation of the observed optical properties may be therefore expected for the spa-ce situation.

3. Multilayer Thin-Films

3.1. Structural and Morphological Changes

In Ref. [72], the structural properties, surface morphology, chemical and phase composition of the Ni 25 nm)/Cu(25 nm)/Cr(25 nm) system under low-energy Ar^+ ion bombardment in the energy range of 400–2000 eV and doses of 1.4×10^{16}–1.1×10^{17} ion·cm^{-2} was studied using XRD, AFM, SEM, AES, XPS, SIMS and SNMS techniques. The thin films were deposited by dc magnetron sputtering at room temperature onto Si(100) substrates. The parameters of Ar^+ ion bombardment are summarised in Table 2. The XRD data of the as-deposited film samples discovered the diffraction peaks corresponding to f.c.c.-Ni, f.c.c.-Cu and b.c.c.-Cr phases. The lattice constants of these phases are a_{Ni} = 0.3526 nm, a_{Cu} = 0.3621 nm, and a_{Cr} = = 0.2888 nm. It was noted that the following Ar^+ ion (<2000 eV) bombardment does not produce any modification of the initial phase composition. The XRD peaks from oxides or other compounds in both as-deposited and

Table 2. **Parameters of the Ar^+ ion bombardment modes [72]**

Mode	Ion energy, eV	Duration, min	Ion dose, ion·cm^{-2}	Mode	Ion energy, eV	Duration, min	Ion dose, ion·cm^{-2}
1	400	40	11.0	5	800	20	5.6
2	600	30	8.4	6	1400	10	2.8
3	600	30	8.4	7	2000	5	1.4
4	800	20	5.6				

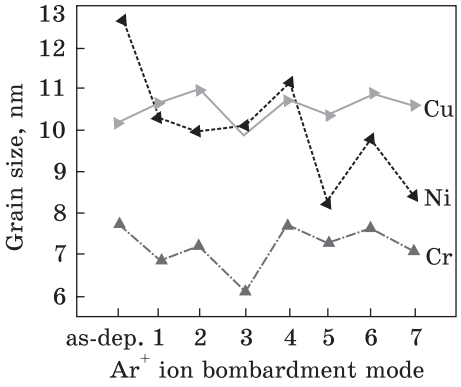

Fig. 20. The averaged grain size of Ni (◄), Cu (►), and Cr (▲) in the as-deposited film and films after Ar^+ ion bombardment with the different modes [72]

ion-irradiated films were not found. However, bombardment with the highest energy of ion beam (2000 eV) leads to a slight decrease of the Ni lattice constant from 0.3526 to 0.3514 nm. Using the XRD the averaged data of each film layer the grain size was calculated (Fig. 20). As a result, the ion does not lead to considerable changes in crystallite size for Cu and Cr films compared to the as-deposited one: the calculated values are 10–11 and 6–7 nm for Cu and Cr films, respectively. At the same time, a decrease of the Ni grain size from ≈13 nm (as-deposited state) to ≈8 nm was established after the 5^{th} and 7^{th} modes, while not so pronounced changes (≈10 nm) were established for other modes.

The ion bombardment-induced of the surface morphological changes occurring in the Cu(40 nm)/Ni(20 nm)/bilayer deposited onto Si(100) by thermal evaporation was investigated in Ref. [73] using the x-ray photoelectron spectroscopy (XPS) and AFM. Bombardment was carried out in the high vacuum using the 3 keV Ar^+ ion beam with current fixed at 10 mA and with the angle of the incidence Ar^+ ion beam on the sample

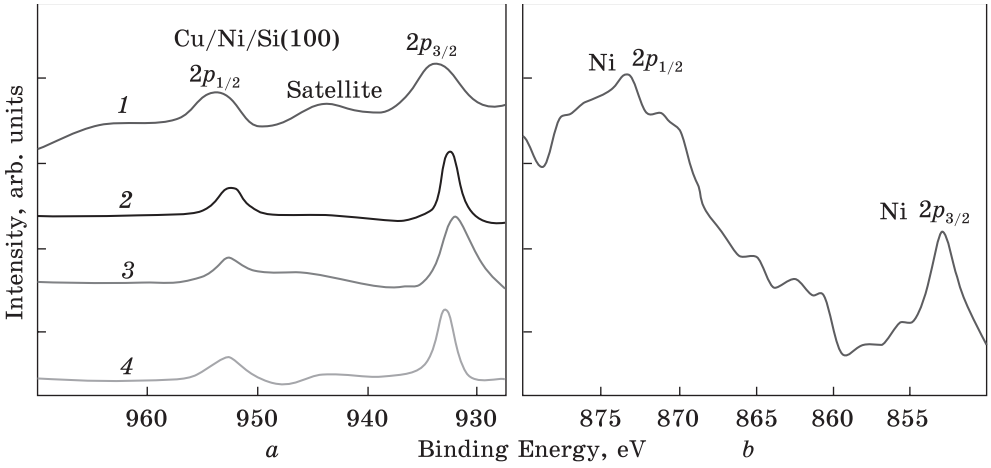

Fig. 21. Cu 2*p* spectra of as-deposited and Ar^+ ion bombarded Cu/Ni/Si(100) films (*a*), where *1* — as deposited, while *2* — 10 min, *3* — 20 min, and *4* — 40 min Ar^+ ion bombardment time. Ni 2*p* spectrum of Cu/Ni/Si(100) films after 40 min Ar^+ ion bombardment (*b*) [73]

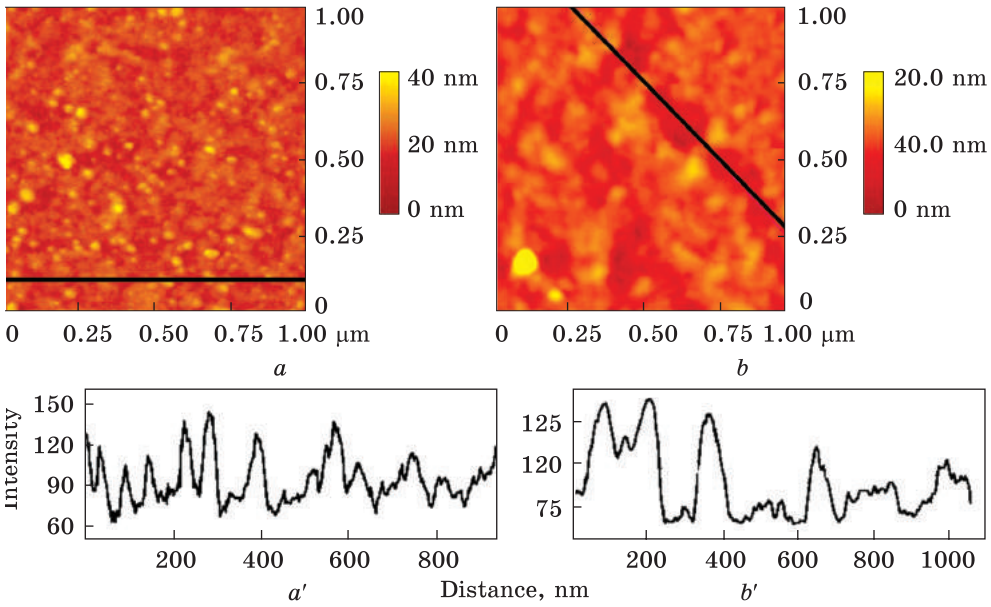

Fig. 22. AFM images of the as-deposited (*a*) and 20 min Ar^+ ion bombarded (*b*) Cu/Ni/Si(100) films along with their line profiles (*a′*, *b′*) [73]

surface about 15° measured from the surface normal of the sample with the dose of 5×10^{15} ions/cm^2. Immediately after the Ar^+ ion, the XPS measurements of Cu 2*p* and Ni 2*p* core levels were carried out at each treatment time. Fig. 21, a shows the evolution of the Cu/Ni bilayer Cu 2*p* core level after Ar^+ ion bombardment with different times as indicated in Fig. 21 (curves *1–4*). The spectrum of the un-bombardment film exhibits four broad features corresponding to main XPS lines 2*p*3/2 and 2*p*1/2 and satellites.

The observed satellite feature indicates that the film surface contains the top CuO layer. After Ar^+ ion bombardment (Fig. 21, *b*) the satellites disappear and the main lines become sharp, indicating the state of the pure metals without oxidation.

The two-dimensional 1000×1000 nm^2 AFM image (upper panel) of the as-deposited Cu/Ni/Si(100) is shown in Fig. 22, *a*. The lower panel of this figure shows sectional relief results along the straight line indicated in the AFM image. These sectional analyses indicate the nanostructure formation on the deposited film with an average particle size of about 40 nm. The two-dimensional 1000×1000 nm^2 AFM images of the film Ar^+ ion bombarded for 10 and 40 min are shown in Fig. 22, *b* and their sectional analyses along the straight lines drawn in the AFM images are shown in Fig. 22, *b′*). After 10 min treatment, the film surface exhibits the structure with an average particle size of about 100 nm. These nanoparticles are of pure Cu. This fact is confirmed by sharp and intense 2*p* peaks of Cu

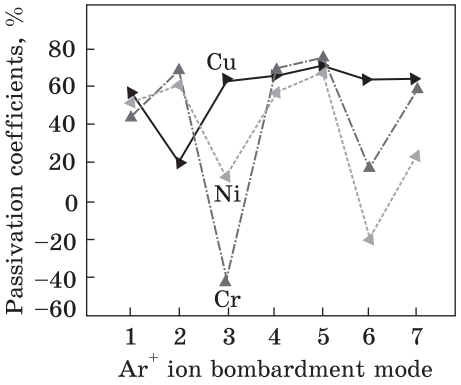

Fig. 23. The passivation coefficients for the Ni (◄), Cu (►), and Cr (▲) thin films after Ar^+ bombardment with the different modes (*1*–*7*) [72]

observed in the XPS spectra for 10 min Ar^+ ion bombardment. After 40 min ion beam treatment, the film surface exhibits large pits of size ranging from 100 to 300 nm with an average depth of about 10 nm.

3.2. Passivation Effect

In Ref. [72] interesting results were obtained also during the study of the oxidation and reduction processes in Ni/Cu/Cr/Si(100) thin films under low-energy Ar^+ ion bombardment. The passivation effect after Ar^+ ion bombardment was investigated using SIMS analysis of the observed secondary metal oxides. Coefficients of the surface passivation K were calculated using the relationship between the current intensities of the secondary oxide ions and corresponding metals [74]. For the Ni thin film, this ratio reads as [74]

$$K_{\mathrm{Ni}} = \left\{\left[(I_{\mathrm{NiO}}/I_{\mathrm{Ni}})_{\mathrm{dep}} - (I_{\mathrm{NiO}}/I_{\mathrm{Ni}})_{\mathrm{bom}}\right]\Big/(I_{\mathrm{NiO}}/I_{\mathrm{Ni}})_{\mathrm{dep}}\right\} \times 100\%,$$

where $(I_{\mathrm{NiO}}/I_{\mathrm{Ni}})_{\mathrm{dep}}$ and $(I_{\mathrm{NiO}}/I_{\mathrm{Ni}})_{\mathrm{bom}}$ are the intensity ratios of NiO and Ni secondary ions received for the as deposited and the ion irradiated films, respectively. The passivation coefficient K for Cr film was determined similarly. Passivation coefficients of Ni and Cr films were found to be the highest after the 2nd and 5th modes of the ion bombardment (Fig. 23), reaching ≈70%. These modes are also considered optimal concerning the Ni film grains size (8–10 nm), sputtering rate and $I_{\mathrm{Cu}(111)}/I_{\mathrm{Ni}(111)} + I_{\mathrm{Cr}(110)}$ intensity ratio. The lowest passivation is observed after the 3rd and 6th modes of the treatment. Moreover, in the case of the 3rd mode, the K_{Cr} shows a negative value, indicating the oxidation process's development. Such processes of the reduction of the oxide at the internal interfaces and, foremost, at the Cr/Si interface are accompanied by the thickening of Cu and Cr films according to the AES and SIMS data of the distribution of the elements. The results obtained are interpreted in terms of the long-range effect of the Ar^+ ion bombardment when the modified layers are away from the bombarded region.

3.3. Removing Impurities

It is important to note that the limitation of the long-term stability of the thin film electric contacts is their possible saturation with light impurities (C, O, *etc*.), which can reduce the device's reliability. Such impurities may be introduced into the thin film structure, for example, during its fabrication or through subsequent exposure to the environment [75]. To avoid introducing the impurities into the thin-film metal structures in Ref. [76], authors studied the effect of the bombardment by the low-energy Ar^+ ions before thermal treatment of the Ni(25 nm)/Cu(25 nm)/V(25 nm) thin-film assembly deposited on the Si(100) substrate using dc magnetron sputtering. The single films for this assembly included Ni as capping, Cu as conducting, and V as the buffer layer. Used two values of the Ar^+ ions energy: 400 eV and 800 eV. After ion bombardment. Thin film samples were annealed at 400 °C (15 min) under Ar pressure at 200 Pa. The pre-bombardment was carried out using Ar^+ ions with a dose of 5.6×10^{16} ion/cm^2 at normal beam incidence. The microstructure, phase, and chemical composition of the thin film samples were examined using XRD, AES, and SIMS.

As shown in the XRD spectra (Fig. 24), the two most prominent Cu and Ni peaks, namely (111) diffraction, could be seen in the range of 42–47°. The XRD spectra for the as-deposited film demonstrated two well-separated peaks (111) of the f.c.c. Ni at 44.613° and f.c.c. Cu at 43.373°. The absence of a V diffraction effect for V is due to the formation of the amorphous state or the ultrafine-grained structure during the deposition. It was observed that the Cu (111) peak shifted towards higher angles at

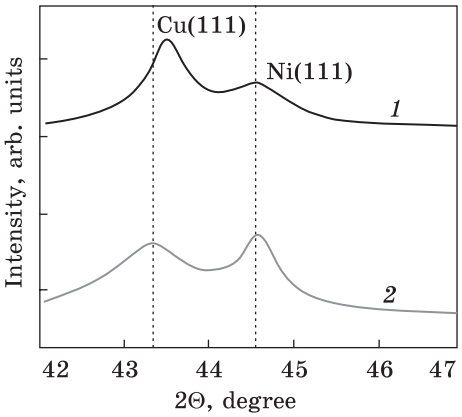

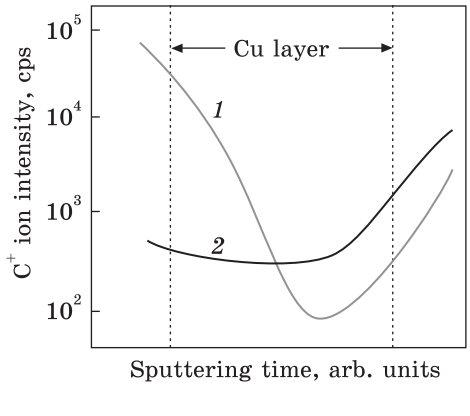

Fig. 24. XRD of the Ni(25 nm)/Cu(25 nm)/V(25 nm) thin films, where *1* — as-deposited and *2* — after 450 °C annealing following by Ar^+ ion bombardment with energy of 800 eV [76]

Fig. 25. Depth distribution of the C^+ secondary ions intensity in the Cu layer region, where *1* — after deposition and *2* — after 450 °C annealing following by Ar^+ ion bombardment with energy of 800 eV [76]

the annealing temperature increased to 300 °C. Such a position indicates the onset of the diffusion reactions between thin layers. Fig. 25 shows the SIMS intensity of the $^{12}C^+$ secondary ions in the Cu region for the as deposited (1) and after 450 °C annealing following Ar^+ ion bombardment with energy 800 eV (2). These results indicate that the intensity of the C atoms in Cu lauer was reduced by 10 times for the 400 eV pre-irradiation and by 100 times for the 800 eV pre-irradiation compared to the regular annealing. Furthermore, it has been shown that after preliminary Ar^+ ion bombardment, the number of oxygen atoms also decreased in the functional Cu region at the subsequent annealing.

3.4. Microtribological Properties

It is important to note that the performance characteristics of the devices using the thin film systems are governed by microtribological properties, namely adhesion between the film and the substrate, wear resistance of the film-substrate system, fracture resistance, and friction coefficient. These properties substantially depend on their structure, surface topography, chemical and phase composition, elastoplastic, and other characteristics of both the films and the substrate [77–81]. Generally accepted tribological tests are successfully accepted for massive materials or thick coatings. However, advanced nanotechnologies require the functional element's thicknesses to decrease to tens or even several nanometers, which significantly complicates the correct examination of the physicomechanical characteristics of such nanosystems. In this regard, we will note the results of the work [82] where the technique of the microtribological test for the nanosize metal thin films was developed for the first time. The microtribological characteristics such as the coefficient of friction, wear resistance, and adhesion were tested for the thin films Cr(30 nm)/Cu(30 nm)/Ni(30 nm)/Si(001) samples in the next states: as-deposited state; after their low-energy ion bombardment; after annealing at 450 °C in vacuum, and finally after their combined treatment when Ar^+ ion bombardment followed by the annealing. Low-energy Ar^+ ion bombardment of the film samples was performed with an energy of 1000 eV and a dose of 5×10^{16} ion/cm^2. Microtribological tests were performed at 300-rpm rotation speed of the precision stage and with the diameter of the track 150 μm. The load on the indenter was gradually increased from zero to 500 mN and then decreased. Such a loading regime allows us to determine the wear resistance, and the critical failure load destroying the thin film from the substrate. In Table 3, the calculated volume losses and the depth of the friction tracks are summarized.

The main result is that the track depth does not exceed the thickness of the original thin film. This experimental fact indicates that the applied load of the microtribological pin-on-disk test directly characterizes the thin films, not the substrate. The film samples after Ar^+ ion bombardment

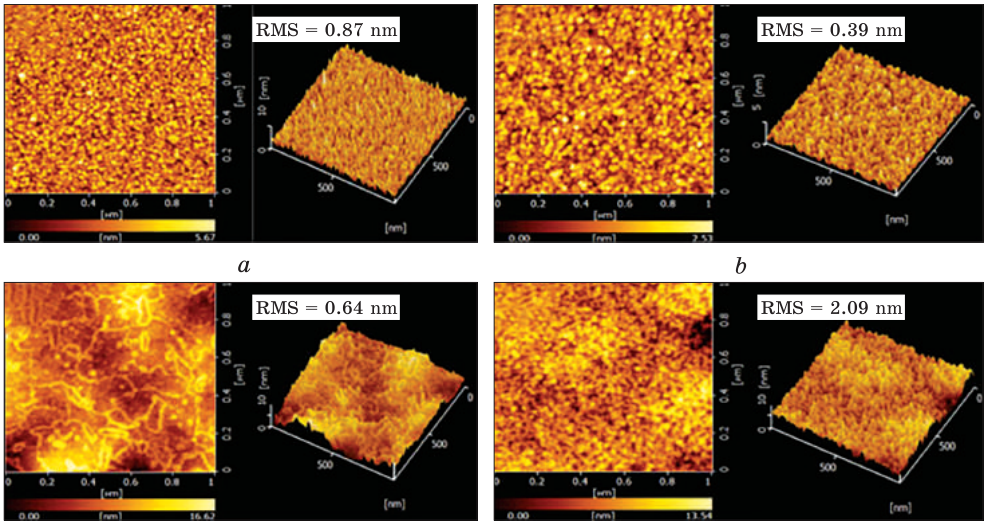

Fig. 26. 3*D* topography images of the wear tracks and friction force of their thin films as a function of the load: as-deposited (*a*), Ar^+ ion bombarded (*b*), annealed (*c*), and annealed with before ion bombardment (*d*) [82]

were destroyed at the lower load of 260 mN that indicates the worst adhesive strength among all the samples was studied. In this case, the formed track had the largest average depth among the studied samples (76 nm).

It was also shown that the application of Ar^+ ion bombardment followed by annealing resulted in substantially improved tribological characteristics. In particular, the film was not destroyed during the test: its friction track depth was only about 27 nm, as well as the wear volume, was the smallest (0.1863×10^6 μm^3) among studied film samples. Fig. 26 demonstrates the AFM images of the surface morphology for the different sample states: the as-received (26, *a*), Ar^+ ion bombarded (*b*), annealed (*c*), and annealed with ion pre-bombardment (*d*). One can that bombardment promotes the sample surface polishing resulting in the halving of the root mean square roughness (RMS) namely (0.39 nm) as compared to the initial

Table 3. **Microtribological characteristics of the studied thin film samples [82]**

Sample	Critical load, mN	Volume loss, μm^3 ($\times 10^6$)	Average track depth, nm
As-deposited	360	0.5808	72
Ion irradiated	260	2.1689	76
Annealed	250	1.0176	72
Annealed with ion pre-irradiation	No destruction	0.1863	27

state (0.87 nm). There is also the interesting fact the heat treatment caused the growth of the grains and the surface irregularities, which was accompanied by an increase of the RMS to 2.64 nm. At the same time, the RMS of the thin sample after complex treatment is slightly lower (2.09 nm).

4. Summary and Conclusions

The single-layer and multi-layer metal nanoscale thin film systems are widely used in the various modern fields of science and technology, in particular, in micro- and nanoelectronics, microsensor technology, spintronic, micro-electromechanical systems, solar energy, *etc*. This is due to their complex being fundamentally different from the massive metal state electronic, magnetic and mechanical properties. To govern the thin film's structure, composition, or functional properties the energetic influences, such as heat treatment and the low energy inert-gas ion bombardment, are usually applied. Such combination methods could significantly change the physic mechanical characteristics of the thin-film materials, affecting the performance and long-term reliability of the final electronic devices. Also special the low-energy interval of the inert-gas ion bombardment is highly attractive for modern thin film technologies as well.

The main results of the most systematic studies of changes in the structure-phase state, the physical, chemical and mechanical properties of the single- and multilayer thin film systems bombarded by the low-energy (<10 eV) inert-gas ions are reviewed and analysed. Analysis of a large number of publications showed that using varying the inert-gas ion beams energy and doses in the low-energy interval, it is possible to control the effectively different properties of the single- or multilayer thin film systems deposited by improving their physical and chemical properties and adhesion processes. The results of such researched systems are described: the single-layer systems are based on such pure metals as Co, Cu, Ni, Pt, Nb, Ti, Fe, and W with thicknesses in the range 25–700 nm; multi-layered thin-films Cu/Ni, Ni/Cu/Cr, Cr/Cu/Ni, and Ni/Cu/V in thickness of each layer 25–30 nm. All films were deposited on the Si(100) substrate. The effect of the inert-gas ions Xe^+, Ar^+, Ne^+, and He^+ with varying beam energy in the range of 200–10000 eV and doses in the range of 10^{15}–10^{19} ions/cm^2 was studied. To study the ion bombardment-induced morphology, microstructure, and chemical and tribological evolution of the polycrystalline thin films were studied using a wide spectrum of methods and tools: x-ray diffraction, secondary ion mass-spectrometry, auger-electron spectroscopy, electrography, transmission electron microscopy, scanning electron microscopy, atomic force microscopy, and tribological tests.

It is possible to note the main scientific results of the analysed publications describing the bombardment complex effects with low-energy inert-gas ions on the structure, chemical, and mechanical properties of the me-

tallic thin film systems. Depending on the bombardment energy and dose it was established the transformation of the grain structure; changes in the surface chemical activity, the optical characteristics, the irradiation-induced stress, the catalytic properties, the electrical resistance, concentration of the light impurities, the patterning self-organization, and the microtribological characteristics.

At last, using varying the inert-gas ion beams energy and doses in the low-energy interval, it is possible to control the effectively different properties of the single- or multilayer thin films deposited systems by improving their physical and chemical properties and adhesion processes. The observed influence effects are of great practical importance in connection with the industry of the high-tech thin-film nanoelectronics elemental base.

Acknowledgement. This publication is based on a work supported through the grant 'Technologies of quantum transport through the interfaces and surfaces of innovative functional thin-film nanostructures created by plasma helicon technologies for the needs of strategic industries and defence' within the budget program КПКВК 6541230 for 2023–2024.

REFERENCES

1. K.L. Chopra, *Thin Film Phenomena* (New York: McGraw-Hill: 1969).
2. Milton Ohring, *The Materials Science of Thin Films* (San Diego: Academic Press: 1992), Ch. 6, p. 249. https://doi.org/10.1016/B978-0-08-051118-4.50012-8
3. Krishna Seshan, *Handbook of Thin Film Deposition Techniques Principles, Methods, Equipment and Applications* (CRC Press: 2002). https://doi.org/10.1201/9781482269680
4. K. Wasa, M. Kitabatake, and H. Adachi, *Thin Film Materials Technology: Sputtering of Compound Materials* (NY, Heidelrberg: William Andrew, Springer: 2004). https://doi.org/10.1016/B978-081551483-1.50002-2
5. King-Ning Tu, *Electronic Thin-Film Reliability* (Cambridge: University Press: 2010).
6. Ludmila Eckertov, Physics of Thin Films (Springer: 2012 p.
7. Kiyotaka Wasa, *Handbook of Sputter Deposition Technology: Fundamentals and Applications for Functional Thin Films, Nano-Materials and MEMS* (William Andrew: 2012).
8. *Thin Film Device Applications* (Eds. Kasturi Lal Chopra and Inderjeet Kaur) (New York: Springer: 1983). https://doi.org/10.1007/978-1-4613-3682-2
9. H. Frey and H.R. Khan, Handbook of Thin-Film Technology (Berlin: Springer: 2015). https://doi.org/10.1007/978-3-642-05430-3
10. L.R. Shaginya, *The Mechanisms of Formation of Thin Films and Coatings Deposited by Physical Vapor Deposition Technology* (Kyiv: PH 'Akademperiodyka': 2017). https://doi.org/10.15407/akademperiodyka.343.174
11. David A. Glocker, *Handbook of Thin Film Process Technology: Reactive Sputtering* (CRC Press: 2018). https://doi.org/10.1201/9781351072793

12. Sam Zhang, Jyh-Ming Ting, and Wan-Yu Wu, *Functional Thin Films Technology* (CRC Press: 2021). https://doi.org/10.1201/9781003088080
13. Jef Poortmans and Vladimir Arkhipov, *Thin Film Solar Cells: Fabrication, Characterization and Applications* (John Wiley & Sons: 2006). https://doi.org/10.1002/0470091282
14. G. Carter, and J.S Colligon, *Ion Bombardment of Solids* (London: Heinemann: 1968).
15. Jerome J. Cuomo, Stephen M. Rossnagel, and Harold R. Kaufman, *Handbook of Ion Beam Processing Technology: Principles, Deposition, Film Modification and Synthesis* (Amsterdam: Elsevier: 1989.).
16. Peter Sigmund, *Sputtering by Ion Bombardment: Theoretical Concepts* (Berlin: Springer: 1981). https://doi.org/10.1007/3540105212_7
17. R.S. Nelson, *The Observation of Atomic Collisions in Crystalline Solids* (Amsterdam: Elsevier: 2013).
18. I. Utke, S. Moshkalev, and P. Russell, *Nanofabrication Using Focused Ion and Electron Beams: Principles and Applications* (Oxford: Oxford University Press: 2012).
19. M. Kaminsky, *Atomic and Ionic Impact Phenomena on Metal Surfaces* (Berlin–Heidelberg: Springer: 1965). https://doi.org/10.1007/978-3-642-46025-8
20. Orlando Auciello and Roger Kelly, *Ion Bombardment Modification of Surfaces: Fundamentals and Applications* (Amsterdam: Elsevier: 1984).
21. Kumar Tanuj, *Nanoscale Pattern Formation under ion bombardment* (Lambert Academic Publishing: 2015).
22. M.O. Vasylyev, S.I. Sidorenko, S.M. Voloshko, and T. Ishikawa, *Usp. Fiz. Met.*, **17**: 209 (2016). https://doi.org/10.15407/ufm.17.03.209
23. S. Ninomiya, K. Ichiki, H. Yamada, Y. Nakata, T. Seki, T. Aokic, and J. Matsuo, *Surf. Interface Anal.*, **43**: 95 (2011). https://doi.org/10.1002/sia.3587
24. M. Sugiyama and G. Sigesato, *J. Electron Microscopy*, **53**: 527 (2004). https://doi.org/10.1093/jmicro/dfh071
25. T.A. Bakhsh, A. Sadr, and J. Tagami, *J. Adhes. Sci. Technol.*, **29**: 232 (2015). https://doi.org/10.1080/01694243.2014.981481
26. A.J.R. van den Boogaard, E. Zoethout, I.A. Makhotkin, E. Louis, and F. Bijkerk, *J. Appl. Phys.*, **112**: 123502 (2012). https://doi.org/10.1063/1.4768915
27. S. Zuccon, E. Napolitani, E. Tessarolo, P. Zuppella, A.J. Corso, F. Gerlin, M. Nardello, and M.G. Pelizzo, *Opt. Mater. Express*, **5**: 176 (2014). https://doi.org/10.1364/OME.5.000176
28. X. Li, K.-W. Lin, H.-T. Liang, H.-F. Hsu, N.G. Galkin, Y. Wroczynskyj, J. Van Lierop, and P.W.T. Pong, *Nucl. Instrum. Methods Phys. Res. Sect. B,* **365**: 196 (2015). https://doi.org/10.1016/j.nimb.2015.07.087
29. L. Repetto, R. Lo Savio, B. Jbetina Batic, G. Firpo, E. Angeli, and U. Valbusa, *Nucl. Instrum. Methods Phys. Res. Sect. B*, **354**: 28 (2015). https://doi.org/10.1016/j.nimb.2014.11.013
30. K. Orlov, I.O. Kruhlov, I.E. Kotenko, S.I. Sidorenko, and S.M. Voloshko, *Metallofiz. Noveishie Tekhnol.*, **39**: 349 (2017). https://doi.org/10.15407/mfint.39.03.0349

31. O.D. Roshchupkina, J. Grenzer, T. Strache, J. McCord, M. Fritzsche, A. Muecklich, and J. Fassbender, *J. Appl. Phys.*, **112**: 033901 (2012). https://doi.org/10.1063/1.4739302
32. S. Zuccon, E. Napolitani, E. Tessarolo, P. Zuppella, A.J. Corso, F. Gerlin, M. Nardello, and M.G. Pelizzo, *Opt. Mater. Express*, **5**: 176 (2014). https://doi.org/10.1364/OME.5.000176
33. Alvin W. Czanderna, Theodore E. Madey, and Cedric J. Powell, Beam Effects, *Surface Topography, and Depth Profiling in Surface Analysis* (Springer: 2006).
34. M. Nastasi, J. Mayer, and J. Hirvonen, *Ion Solid Interactions: Fundamentals and Applications* (Cambridge: University Press: 1996). https://doi.org/10.1017/CBO9780511565007
35. R.K. Sherburne and H.E. Farnsworth, *J. Chem. Phys.*, **19**: 387 (1951). https://doi.org/10.1063/1.1748229
36. R. Miranda, J.M. Rojo, and M. Salmeron, *Solid State Comm.*, **35**: 83 (1980). https://doi.org/10.1016/0038-1098(80)90777-2
37. L. Gonzalez, R. Miranda, and S. Ferrer, *Solid State Comm.*, **44**: 1461 (1982). https://doi.org/10.1016/0038-1098(82)90031-X
38. R. Miranda and J. M. Rojo, *Vacuum*, **34**: 1069 (1984). https://doi.org/10.1016/0042-207X(84)90227-6
39. S.P. Chenakin, *Vacuum*, **36**: 635 (1986). https://doi.org/10.1016/0042-207X(86)90332-5
40. S.P. Chenakin, *Appl. Surface Sci.*, **84**: 91 (1995). https://doi.org/10.1016/0169-4332(94)00471-4
41. S. Rusponi, G. Costantini, C. Boragno, and U. Valbusa, *Phys. Rev. Lett.*, **81**: 4184 (1998). https://doi.org/10.1103/PhysRevLett.81.4184
42. M.V. Ramana Murty, T. Curcic, A. Judy, B.H. Cooper, A.R. Woll, J.D. Brock, S. Kycia, and R.L. Headrick, *Phys. Rev. B*, **60**: 16956 (1999). https://doi.org/10.1103/PhysRevB.60.16956
43. S. Rusponi, C. Boragno, and U. Valbusa, *Phys. Rev. Lett*, **78**: 2795 (1997). https://doi.org/10.1103/PhysRevLett.78.2795
44. Wai Lun Chan, and Eric Chason, *J. Appl. Phys.*, **101**: 121301 (2007). https://doi.org/10.1063/1.2749198
45. A.J.R. van den Boogaard, E. Zoethout, I.A. Makhotkin, E. Louis, and F. Bijkerk, *J. Appl. Phys.*, **112**: 123502 (2012). https://doi.org/10.1063/1.4768915
46. S. Zuccon E. Napolitani, E. Tessarolo, P. Zuppella, A. J. Corso, F. Gerlin, M. Nardello, and M. G. Pelizzo, *Opt. Mater. Express*, **5**: 176 (2014). https://doi.org/10.1364/OME.5.000176
47. X. Li, K.W. Lin, H.T. Liang, H.F. Hsu, N.G. Galkin, Y. Wroczynskyj, J. van Lierop, and P.W.T. Pong, *Nucl. Instrum. Methods Phys. Res. B*, **365**: 196 (2015). https://doi.org/10.1016/j.nimb.2015.07.087
48. S.L. Repetto, R. Lo Savio, B. Šetina Batic, G. Firpo, and U. Valbusa, *Nucl. Instrum. Methods Phys. Res. B*, **354**: 28 (2015). https://doi.org/10.1016/j.nimb.2014.11.013
49. M. Marinov and D. Dobrev, *Thin Solid Films*, **42**: 265 (1977). https://doi.org/10.1016/0040-6090(77)90361-3
50. Y. Hasegawa, Y. Fujimoto and F. Okuyama, *Surf, Sci.*, **163**: L781 (1985). https://doi.org/10.1016/0167-2584(85)90883-7
51. M. Tanemura, *Nucl. Instrum. Methods Phys. Res. B*, **47**: 126 (1990). https://doi.org/10.1016/0168-583X(90)90020-U

52. A.D.G. Stewart and M.W. Thompson, *J. Mater. Sci.*, **4**: 56 (1969). https://doi.org/10.1007/BF00555048
53. M.J. Nobes, J.S. Colligon, and G. Carter, *J. Mater. Sci.*, **4**: 730 (1969). https://doi.org/10.1007/BF00742430
54. J.P. Ducommun, M. Cantagrel, and M. Marchal, *J. Mater. Sci.*, **9**: 725 (1974). https://doi.org/10.1007/BF00761792
55. Y. Hasegawa, Y. Fujimoto, and F. Okuyama, *Surf. Sci.*, **163**: 781 (1985). https://doi.org/10.1016/0167-2584(85)90883-7
56. S. Blazhevich, N. Kamyshanchenko, I. Martynov, and I. Neklyudov, *Nucl. Instrum. Methods Phys. Res. B*, **193**: 312 (2002). https://doi.org/10.1016/S0168-583X(02)00797-8
57. G.S. Tang, H.Y. Liu, F. Zeng, and F. Pan, *Vacuum*, **89**: 157 (2013). https://doi.org/doi:10.1016/j.vacuum.2012.03.039
58. G. Ozaydin, K.F. Ludwig, Jr., H. Zhou, R.L. Headrick, *J. Vac. Sci. Technol. B*, **26**: 551 (2008). https://doi.org/10.1116/1.2870222
59. T.G. Bifano, H.T. Johnson, P. Bierden, and R.J. Mali, *J. Microelectromech. Syst.*, **11**: 592 2002. https://doi.org/10.1109/JMEMS.2002.802908
60. E. Chason, S.T. Picraux, J.M. Poate, J.O. Borland, M.T. Current, T.D. de la Rubia, D.J. Eaglesham, O.W. Holland, M.E. Law, C.W. Magee, J.W. Mayer, J. Melngailis, and A.F. Tasch, *J. Appl. Phys.*, **81**: 6513 (1997). https://doi.org/10.1063/1.2749198
61. W.-L. Chan, K. Zhao, N. Vo, Y. Ashkenazy, D.G. Cahill, and R.S. Averback, *Phys. Rev B*, **77**: 205405 (2008). https://doi.org/10.1103/PhysRevB.77.205405
62. S.-H. Lee, E.-H. Kwak, H.-S. Kim, S.-W. Lee, and G.-H. Jeong, *Thin Solid Films*, **547**: 188 (2013). https://doi.org/10.1016/j.tsf.2013.03.064
63. M.O. Vasylyev, S.I. Sidorenko, I.O. Kruhlov, and D.I. Trubchaninova, *Metallofiz. Noveishie Tekhnol.*, **42**, No. 5: 621 (2020) (in Ukrainian). https://doi.org/10.15407/mfint.42.05.0621
64. A. Benninghoven, *Surf. Sci.*, **35**: 427 (1973). https://doi.org/10.1016/0039-6028(73)90232-X
65. E. Stumpe and A. Benninghoven, *Phys. Status Solidi A*, **21**: 479 (1974). https://doi.org/10.1002/pssa.2210210212
66. V.T. Cherepin, M.O. Vasylyev, I.M. Makeeva, V.M. Kolesnik, and S.M. Voloshko, *Prog. Phys. Met.*, **19**, No. 1: 49 (2018). https://doi.org/10.15407/ufm.19.01.049
67. S.E. Donnelly, F. Bodart, K.M. Barfoot, R. Werz, and R.P. Webb, *Thin Solid Films*, **94**: 289 (1982). https://doi.org/10.1016/0040-6090(82)90491-6
68. B. Navinsek and G. Carter, Canadian *J. Phys.*, **46**:719 (1968). https://doi.org/10.1139/p68-088
69. B. Navinsek and G. Carter, *Appl. Phys. Lett.*, **10**: 91 (1967). https://doi:10.1063/1.1754865
70. M. Deery, K.H. Goh, K.G. Stephens, and I.H. Wilson, *Thin Solid Films*, **17**: 59 (1973). https://doi.org/10.1016/0040-6090(73)90005-9
71. S. Zuccon, E. Napolitani, E. Tessarolo, P. Zuppella, A.J. Corso, F. Gerlin, M. Nardello, and M.G. Pelizzo, *Optical Mater. Express*, **5**: 176 (2015). https://doi.org/10.1364/OME.5.000176

72. I.O. Kruhlov, I.A. Vladymyrskyi, O. Dubikovskyi, S.I. Sidorenko, T. Ebisu, K. Kato, O. Sakata, T. Ishikawa, Y. Iguchi, and G.A. Langer, *Mater. Res. Express*, **6**: 126431 (2019).
https://doi.org/10.1088/2053-1591/ab6382
73. S.K. Parida, V.R. Rmedicherla, D.K. Mishra, S. Choudhary, V. Solanki, and S. Varma, B*ull. Mater. Sci.*, **37**: 1569 (2014).
https://doi.org/10.1007/s12034-014-0727-5
74. S.P. Chenakin, *Vacuum*, **36**: 635 (1986).
https://doi.org/10.1016/0042-207X(86)90332-5
75. L. De Los Santos Valladares, D. Hurtado Salinas, A. Bustamante Dominguez, D. Acosta Najarro, S.I. Khondaker, T. Mitrelias, C.H.W. Barnes, J. Albino Aguiar, and Y. Majima, *Thin Solid Films*, **520**: 6368 (2012).
https://doi.org/10.1016/j.tsf.2012.06.043
76. O. Kruhlov, A.K. Orlov, O. Dubikovskyi, Y. Iguchi, Z. Erd´elyi, S.I. Sidorenko, T. Ishikawa, S.V. Prikhodko, and S.M. Voloshko, *Materials Today Communications*, **34**: 104977 (2023).
https://doi.org/10.1016/j.mtcomm.2022.104977
77. S.A. Firstov, S.R Ignatovich, and I.M. Zakiev, *Strength Mater.*, **41**: 147 (2009).
https://doi.org/10.1007/s11223-009-9116-5
78. V.A. Mechnik, N.A. Bondarenko, V.M. Kolodnitskyi, V.I. Zakiev, I.M. Zakiev, S.R. Ignatovich, and N.O. Kuzin, *Powder Metall. Met. Ceram.*, **58**: 679 (2020).
https://doi.org/10.1007/s11106-020-00125-w
79. V.G. Efremenko, Y.G. Chabak, V.I. Fedun, K. Shimizu, T.V. Pastukhova, I. Petryshynets, and B.V. Efremenko, *Vacuum*, **185**: 110031 (2021).
https://doi.org/10.1016/j.vacuum.2020.110031
80. I. Zakiev, M. Storchak, G.A. Gogotsi, V. Zakiev, and Y. Kokoieva, *Ceramics Int.*, **47**: 29638 (2021).
https://doi.org/10.1016/j.ceramint.2021.07.133
81. V. Zakiev, A. Markovsky, E. Aznakayev, I. Zakiev, and E. Gursky, *Medical Imaging. International Society for Optics and Photonics*, **5959**: 595916 (2005).
82. I. Kruhlov, A. Orlov, V. Zakiev, I. Zakiev, S. Prikhodko, and S. Voloshko, TMS 2022 151st Annual Meeting & Exhibition Supplemental Proceedings. *The Minerals, Metals & Materials Series* (Cham: Springer: 2022), p. 431.
https://doi.org/10.1007/978-3-030-92381-5_39

Received 25.11.2023
Final version 19.04.2024

М.О. Васильєв[1], *Е.М. Руденко*[1], *С.М. Волошко*[2]
[1] Інститут металофізики ім. Г.В. Курдюмова НАН України,
бульв. Академіка Вернадського, 36, 03142 Київ, Україна
[2] Національний технічний університет України
«Київський політехнічний інститут імені Ігоря Сікорського»,
пр. Перемоги, 37, UA-03056 Київ, Україна

ВПЛИВ НИЗЬКОЕНЕРГЕТИЧНОГО БОМБАРДУВАННЯ ІОНАМИ ІНЕРТНОГО ГАЗУ НА СТРУКТУРУ ТА ВЛАСТИВОСТІ МЕТАЛЕВИХ ТОНКИХ ПЛІВОК

Метою огляду є аналіз основних опублікованих результатів найбільш систематичних досліджень зміни структурно-фазового стану, фізико-хімічних властивостей систем металевих одно- та багатошарових тонких плівок після бомбардування низькоенергетичними (<10 еВ) іонами інертного газу. Нанорозмірні плівкові систе-

ми було одержано за допомогою двох поширених фізичних методів: магнетронного осадження та терморезистивного випаровування. В основі одношарових систем лежать такі чисті метали, як Co, Cu, Ni, Pt, Nb, Ti, Fe, W. Нанесені на підкладинку Si(100) плівки мали товщину в діапазоні 25–700 нм. Багатошарові тонкі плівки виготовлено на основі таких комбінацій: Cu/Ni, Ni/Cu/Cr, Cr/Cu/Ni і Ni/Cu/V з товщиною кожного шару у 25–30 нм. Застосовували низькоенергетичне бомбардування іонами інертного газу (Xe^+, Ar^+, Ne^+, He^+) зі зміною енергії пучка в діапазоні 200–10 000 еВ і флюенсом у діапазоні 10^{15}–10^{19} іонів/см^2. Морфологію, мікроструктуру та хімічну еволюцію полікристалічних тонких плівок, спричинену іонним бомбардуванням, досліджували за допомогою рентгенівської дифракції, вторинної іонної масспектрометрії, оже-електронної спектроскопії, електрографії, трансмісійної електронної мікроскопії, сканувальної електронної мікроскопії, атомно-силової мікроскопії та трибологічних випробувань. Обговорюються різні фізичні механізми, що сприяють цій еволюції, та їхній зв'язок із теоретичними моделями й експериментальними дослідженнями тонких плівок, індукованих іонами.

Ключові слова: тонкі плівки, іонне бомбардування, поверхні, фазові перетворення, зносостійкість.